Navigating Complex Phase Diagrams in Soft Matter Systems

Michael Wassermair,[1,2,3] Gerhard Kahl,[1] Roland Roth,[4] and Andrew J. Archer[2]
[1]Institut für Theoretische Physik, TU Wien, Wiedner Hauptstraße 8-10, A-1040 Vienna, Austria
[2]Department of Mathematical Sciences and Interdisciplinary Centre for Mathematical Modelling, Loughborough University, Loughborough LE11 3TU, United Kingdom
[3]Institute of Science and Technology Austria, 3400 Klosterneuburg, Austria
[4]Institute for Theoretical Physics, University of Tübingen, D-72076 Tübingen, Germany

(Received 24 November 2025; accepted 12 March 2026; published 10 April 2026)

Colloidal fluids can exhibit complex phase behavior and determining phase diagrams via experiments or computer simulations can be laborious. We demonstrate that the dispersion relation $\omega(k)$, obtained from dynamical density functional theory for the uniform density system, is a highly versatile tool for *predicting* where in the phase diagram complex crystals form. The sign of $\omega(k)$ determines whether density modes with wave number k grow or decay over time. We demonstrate the predictive power by investigating the complex phase behavior of particles interacting via core-shoulder pair potentials. With complementary Monte Carlo simulations, we show that regions of the phase diagram where $\omega(k)$ has one or several unstable (growing) wave numbers are also where crystalline phases occur. Going further, by tuning these unstable wave numbers via the interaction-potential and state-point parameters, we design systems with quasicrystals in the phase diagram. We identify a system with a certain shoulder range exhibiting at least ten different phases. Our general approach accelerates considerably the mapping of complex phase diagrams, crucial for the design of new materials.

DOI: 10.1103/nbvt-fgjy

Self-assembly into complex structures underpins much of soft-matter, materials, and condensed-matter science. Collections of particles with relatively simple interactions, such as attractive wells, repulsive ramps, and/or square shoulder systems, are capable of generating a variety of complex structures [1,2]. A fascinating and useful property of soft-matter and colloidal systems is that the potentials between the particles can be tuned in a seemingly unlimited manner by the chemistry and geometry of the constituent molecules, especially those on the surfaces of the particles [3,4]. For example, by grafting polymers onto the surface of colloidal spheres, core-shell particles are created that assemble into a wide variety of structures, determined by the polymer lengths and grafting density [5–9]. This control enables the formation of structures with designed symmetries, and optical and other properties, for numerous applications [10].

Determining the phase diagram, specifically mapping where the solid crystalline, or even quasicrystalline (QC) phases arise, is crucial for designing new materials [11]. This effort can be expensive and time consuming to realize in experiments. Computer simulations can be cheaper, but often still prolonged. Thus, the predictive theory we develop, albeit one that does not give the full answer, to identify where the solid phases arise is very powerful. We show how a purely analytic, computationally cheap theory for the growth or decay of density perturbations is able to guide Monte Carlo (MC) computer simulations to the relevant portions of the phase diagram, saving much effort. Our theory is based on classical density functional theory (DFT) [12–14] and its dynamical extension, DDFT [14–17]. We demonstrate the effectiveness of our approach by applying it to systems of core-shell particles, which (we show) can exhibit complex phase diagrams. We present a two-dimensional (2D) example with at least ten different phases. We expect our general approach to become a widely applicable initial-survey tool for mapping soft-matter phase diagrams.

We demonstrate our approach for 2D systems interacting via the hard-core, square-shoulder (HCSS) pair potential $\phi(r) = \phi_\sigma(r) + \epsilon H(\lambda\sigma - r)$, where $\phi_\sigma(r)$ is the hard-disks potential with diameter σ and $\epsilon H(\lambda\sigma - r)$, with the Heaviside function $H(r)$, is a square shoulder potential with range $\lambda\sigma$ and interaction strength $\epsilon > 0$. The state of the system is determined by the dimensionless density $\rho_b^\star = \rho_b\sigma^2$ (with corresponding packing fraction $\eta = \pi\rho_b^\star/4$), where ρ_b is the average bulk density, and dimensionless temperature $T^\star = k_B T/\epsilon$, where k_B is Boltzmann's constant and T is the temperature. Henceforth, we set $\sigma = 1$,

Published by the American Physical Society under the terms of the Creative Commons Attribution 4.0 International license. Further distribution of this work must maintain attribution to the author(s) and the published article's title, journal citation, and DOI.

$k_B T = \beta^{-1} = 1$ and drop the $\star$ superscript, so that $T = 1/\epsilon$.

Despite the simplicity, HCSS particles can self-assemble into a plethora of different phases involving single or multiple characteristic length scales and varying levels of complexity [8,18–25]. There is no gas-liquid phase transition, but on increasing η at sufficiently low T, one typically observes cluster, stripe, and hole phases, with details depending greatly on λ. Many other different phases can also be observed either instead of or as well, including QCs [22–24].

The importance of identifying the wavelength ℓ of the periodic modulations in the equilibrium density distribution $\rho_0(\mathbf{r})$ of crystalline structures has long been understood [26]. Building on such ideas, soft pair potentials have been designed so that the particles self-assemble into a variety of QCs and other structures [27–34]. QCs arise from the coupling of density modes with wave numbers $k_1 = 2\pi/\ell_1$ and $k_2 = 2\pi/\ell_2$, with ratio k_1/k_2 taking specific values [35]. It was also observed that the liquid state static structure factor $S(k)$ [14] can be used to identify the specific k_i that, when the system is cooled below the freezing point, govern the crystalline phases [36]. These ideas are the background to the present theory that enables navigation of complex phase diagrams and provides a basis for designing interaction potentials that give rise to specified self-assembled structures.

The start point is to analyze the nonequilibrium dynamics of a homogeneous bulk liquid with density ρ_b, following a quench to a certain temperature T. If this quench is to a state point where the liquid is unstable, the density distribution becomes heterogeneous $\rho(\mathbf{r}, t)$, evolving in time t toward the equilibrium $\rho_0(\mathbf{r})$, governed by the continuity equation $(\partial\rho/\partial t) = -\nabla \cdot \mathbf{j}$, where $\mathbf{j}(\mathbf{r}, t)$ is the current. DDFT [14–17] provides a good approximation for $\mathbf{j}$, as long as a reliable approximation is available for the grand potential functional

$$\Omega[\rho] = F_{\mathrm{id}}[\rho] + F_{\mathrm{ex}}[\rho] + \int \rho(\mathbf{r})(V_{\mathrm{ext}}(\mathbf{r}) - \mu)\mathrm{d}\mathbf{r}, \quad (1)$$

where $F_{\mathrm{id}}[\rho]$ is the ideal-gas contribution, $F_{\mathrm{ex}}[\rho]$ is the excess Helmholtz free energy that depends on the nature of the particle interactions, $V_{\mathrm{ext}}(\mathbf{r})$ is the external potential (here assumed to be zero), and μ is the chemical potential [12,14]. For particles with overdamped stochastic (Brownian) equations of motion, DDFT gives

$$\mathbf{j} = \Gamma\rho\nabla\frac{\delta\Omega[\rho]}{\delta\rho}, \quad (2)$$

where $\Gamma = D/k_B T$ is the mobility coefficient, with D the diffusion coefficient [14–17]. For dense atomic or molecular fluids, where the particles evolve under Newton's equations of motion, it turns out that (2) still provide a reasonable description [37,38], as long as the system is not too far from equilibrium. The density distribution of the quenched liquid is never perfectly uniform; it must have small amplitude random density perturbations $\tilde{\rho}(\mathbf{r}, t) \equiv \rho(\mathbf{r}, t) - \rho_b$ around the average value, ρ_b. To investigate the initial growth/decay dynamics of such perturbations after the quench, it suffices to consider the linearized form of the continuity equation, $(\partial\tilde{\rho}/\partial t) = \mathcal{L}\tilde{\rho} + \mathcal{O}(\tilde{\rho}^2)$. Here, $\mathcal{L}$ is a linear operator obtained from performing a functional Taylor expansion of Eq. (2) in powers of $\tilde{\rho}$. We obtain $\mathcal{L} = D\nabla^2 - D\rho_b\nabla^2 c^{(2)} \otimes$, with $\otimes$ denoting convolution, i.e., $c^{(2)} \otimes \tilde{\rho} \equiv \int d\mathbf{r}' c^{(2)}(\mathbf{r} - \mathbf{r}')\tilde{\rho}(\mathbf{r}', t)$, and where $c^{(2)} \equiv -\beta\delta^2 F_{\mathrm{ex}}/\delta\rho^2$ is the pair direct correlation function (pDCF) [14,16]. In the liquid, the pDCF may instead be obtained via the Ornstein-Zernike equation [14]. We introduce the dispersion relation $\omega(k)$ by decomposing the perturbation $\tilde{\rho}$ into its Fourier components

$$\tilde{\rho}(\mathbf{r}, t) = \sum_{\mathbf{k}} \hat{\rho}_{\mathbf{k}} e^{i\mathbf{k}\cdot\mathbf{r} + \omega(k)t}, \quad (3)$$

where $k \equiv |\mathbf{k}|$, $\hat{\rho}_{\mathbf{k}}$ are the $(t = 0)$ initial amplitudes and thus (depending on the sign) $\omega(k)$ is the growth/decay rate of each mode [note our definition of $\omega(k)$ following, e.g., [39,40], *without* prefactor $i = \sqrt{-1}$]. From the linearized dynamics, the dispersion relation is obtained in terms of the Fourier transform of the pDCF $\hat{c}(k)$ as

$$\omega(k) = -Dk^2[1 - \rho_b\hat{c}(k)]. \quad (4)$$

In an equilibrium liquid $S(k) = 1/[1 - \rho_b\hat{c}(k)]$, so in this case $\omega(k) = -Dk^2/S(k) \leq 0$, for all k. In regions of the phase diagram where solid phases arise (where the liquid is either unstable or metastable) we obtain $\hat{c}(k)$ *generated* by DFT. This relies on having a suitable approximation for F_{ex}. However, as we show, even with an approximate functional that does not always distinguish correctly *all* the different crystal phases, we still find that the resulting $\omega(k)$ reliably estimates the locations in the phase diagram where the solid phases arise. The approximation for F_{ex} used here is a standard mean-field approximation, splitting it into a hard-disk part, treated using fundamental measure theory [41,42], plus a random-phase approximation (RPA) for the shoulder part. Further details are in Supplemental Material [43], including an analytic expression for $\hat{c}(k)$ [45]. Note that $\omega(k)$ effectively depends solely on thermodynamic structural quantities, therefore our analysis is independent of the assumed dynamics (Brownian or Newtonian).

By elementary analysis of $\omega(k)$ we can identify regions in the phase diagram where the liquid is stable by determining if $\omega(k) \leq 0$ for all k. Consequentially, in regions where $\omega(k) > 0$ for some k, the formation of structured phases is to be expected. At high T, on increasing η, this is precisely what we observe. However, at lower η (and low T) there is a subtlety to making this analysis with a dispersion relation

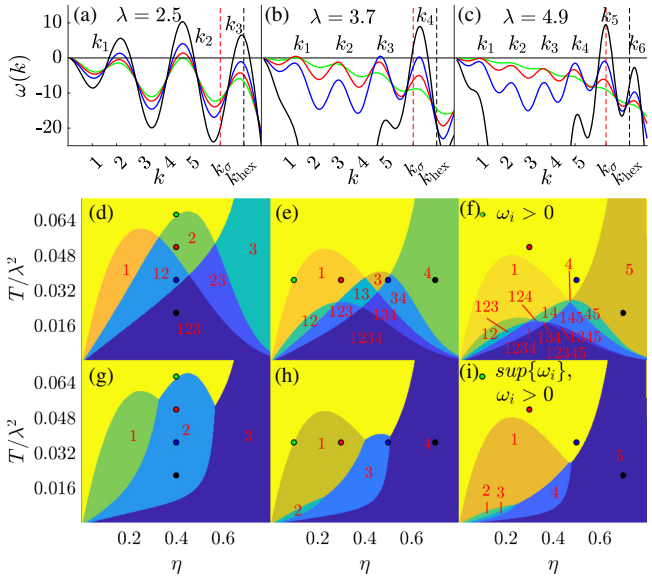


FIG. 1. Top row: dispersion relation $\omega(k)$ for the HCSS system for (a) $\lambda = 2.5$, (b) $\lambda = 3.7$, and (c) $\lambda = 4.9$. The maxima at k_i (with $i = 1, 2, 3, \ldots$) are indicated. The state points at which $\omega(k)$ is evaluated are the correspondingly colored dots in the $(T/\lambda^2, \eta)$-plane diagrams below each, labeled (d)–(i). The red and black vertical dashed lines indicate the characteristic core-diameter wave number $k_\sigma = 2\pi$ (with $\sigma = 1$) and the hexagonal close packing wave number $k_{\text{hex}} = 4\pi/\sqrt{3}$, respectively. The phase diagrams (d)–(f) show where each of the different maxima k_i are positive $\omega(k_i) = \omega_i > 0$ (the numbers i in each region are the positive peak indices), while diagrams (g)–(i) show regions where each of the different maxima are the supremum, $\sup\{\omega_i\}, \omega_i > 0$. In the yellow regions, $\omega(k) \leq 0$ for all k.

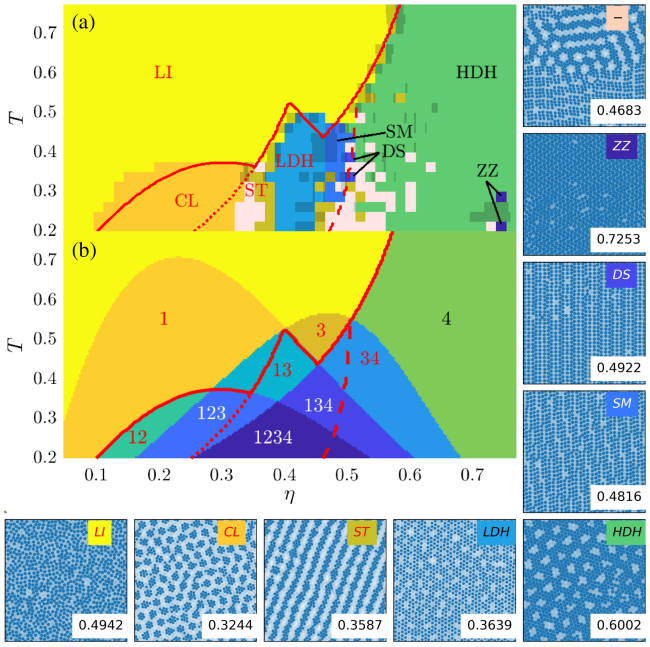


FIG. 2. (a) Phase diagram of the HCSS system for $\lambda = 3.7$ obtained via GEMC. Each pixel represents an individual GEMC simulation. For each we plot either (i) the color of the phase if both simulation boxes contain the same phase, or (ii) the color of the denser phase and the extent of the coexistence region (as a gray shaded area) if phase coexistence is observed, or (iii) plot the pixel pale pink in cases where simulations were indecisive, i.e., we found more than one phase in one of the simulation boxes, such as the example labeled "-" at top right. The color coding corresponds to the color of the labels in the single GEMC simulation box snapshots displayed along the bottom and on the right. The naming acronyms are defined in the text, while the numbers on each are the η values. (b) The corresponding region of Fig. 1(e), showing how boundaries between the different regions (red lines) match with the phase boundaries in panel (a) diagram. The red lines are either boundary lines where a second mode ω_i becomes unstable, or lines where two maxima are equal, $\omega_i = \omega_j$, $i \neq j$; i.e., boundaries from Fig. 1(h). Specifically, the dotted and dashed lines are where $\omega_2 = \omega_3$ and $\omega_3 = \omega_4$, respectively.

$\omega(k)$ obtained from a mean-field approximate DFT: What we actually find here is that when $\omega(k)$ exhibits only one small positive peak (i.e., only one weakly unstable mode) then MC simulations show that the system can in fact still be in the disordered liquid state, albeit this liquid is highly correlated, with clear signature of the favored length scale. In other words, although the linearized mean-field functional predicts the liquid to be unstable and the solid to form, in reality thermal fluctuations are strong enough to prevent freezing in this regime. At lower η, it is only when $\omega(k)$ exhibits at least two positive peaks that periodic (or QC) phases are found as the thermodynamic equilibrium state. Moreover, the locus in the phase diagram where the additional k_i become unstable is close to the coexistence line between the liquid and crystalline phases, as identified from the MC simulations. Thus, the line in the phase diagram where there are multiple unstable modes k_i provides a good estimate for where freezing occurs at low η. We illustrate this in Figs. 1 and 2. We believe more than one unstable mode in $\omega(k)$ is required for crystals (or QC) to be stable at low η because at these densities the structures are rather open (with plenty of free space) and so require the coupling of periodic density modes with more than one wavelength to stabilize them.

Figures 1(a)–1(c) show typical examples of $\omega(k)$ for three different shoulder ranges, $\lambda = 2.5$, 3.7, and 4.9. The shoulder height $\epsilon = 1/T$ and the packing fraction η can be identified from the position of the correspondingly colored dots in the diagrams below each in panel (d)–(i). The relevant range is $k \in (0, k_{\text{hex}})$, where $k_{\text{hex}} = 4\pi/\sqrt{3}$ is the wave number corresponding to hexagonal close packing of hard discs with diameter $\sigma = 1$ (vertical black dashed line). The other relevant scale is $k = 2\pi/\sigma$, marked as a vertical red dashed line. The locations of the peaks in $\omega(k)$ are denoted by the peak-value wave numbers k_i (where $i = 1, 2, 3, \ldots$), with $\omega_i = \omega(k_i)$. These arise from an interplay between oscillations in $\omega(k)$ arising from the hard-core interactions with those due to the shoulder-interactions, having amplitude proportional to ϵ. As shown in Figs. 1(a)–1(c), for $\lambda = 2.5$, $\lambda = 3.7$, and $\lambda = 4.9$, there

are three, four, and five possible unstable modes k_i, respectively. Note for $\lambda = 4.9$, $k_6 > k_{\rm hex}$.

Following three different pathways through the (T, η) plane, we observe the following trends: (i) On decreasing T—see Figs. 1(a), 1(d), and 1(g)—we find the maxima of $\omega(k)$ increasing, till they eventually become positive in value. (ii) Keeping T fixed and increasing η—see Figs. 1(b), 1(e), and 1(h)—we observe a shift upward in $\omega(k)$ at higher k. For $\lambda = 3.7$ this leads to the emergence of a single dominant peak at $k_4 \approx k_\sigma = 2\pi$, the characteristic wave number of the hard core. For even higher densities, k_4 tends toward $k_{\rm hex}$, converging at $\eta \approx 0.904$. The increase of $\omega_4 = \omega(k_4)$ is accompanied by a suppression of the growth rates ω_i for $i < 4$. This can even lead to the disappearance of peaks at smaller k—see, e.g., for k_1 at $\eta = 0.7$ (black line). Note that while the k_4 peak shifts with varying η, the positions k_i of the other peaks do not change significantly, due to the quadratic density dependency of the RPA shoulder-interaction part of $F_{\rm ex}$. (iii) In Figs. 1(c), 1(f), and 1(i) we observe a somewhat similar behavior on a diagonal path in the phase diagram for $\lambda = 4.9$, with the k_5 peak growth rate $\omega_5 = \omega(k_5)$ increasing with increasing η.

In Fig. 2 we revisit the $\lambda = 3.7$ phase diagram [see Fig. 1(e)], complemented by snapshots of some of the phases found. Panel (a) summarizes the outcome of scanning through parameter values with Gibbs ensemble MC (GEMC) to identify the phases that arise [46]. Figure 2(b) is the corresponding region from Fig. 1(e), showing where the ω_i of the various peaks k_i are positive. The red lines show where some of the ω_i either change sign or where $\omega_i = \omega_j$ with $i \neq j$ (see caption). Note that these line up rather well with the freezing boundaries. Along the bottom and right of Fig. 2 are examples of some of the phases observed, labeled with combinations of letters to indicate the various phases and background color corresponding to the color used in the top phase diagram. For example, "LI" refers to the liquid phase and is colored yellow. At lower η, structured phases occur at low T and are primarily shaped by the long-wavelength k_1 mode [e.g., the cluster (CL) and stripe (ST) phases]. The region where ω_3 is largest is predominantly populated by the low-density-hole LDH phase, dominated by density modulations with wave number k_3 (also see Fig. 3). Along the red dashed line in Fig. 2 the balanced competition between the k_3 and k_4 modes leads to a particularly rich phase behavior and the occurrence of several phases involving both modes, such as the striped smectic (SM) and double-stripe (DS) structures, as well as the rhombic phase observed in grand canonical MC (GCMC) simulations [see Fig. 3(c)], not resolved with GEMC. At higher η, we find excellent correspondence between where $\omega_4 > 0$ and the region of the high-density-hole (HDH) phase, dominated by the k_4 mode. The closeness of the LI-HDH phase transition to the $(\omega_4 = 0)$ line highlights the predictive capabilities of the theory. At very high densities we also encountered a zigzag phase—cf. Refs. [50,51]. Overall, we see that our simple theory based on $\omega(k)$ can quickly predict (i) where to look for crystalline phases and (ii) what combinations of length scales to expect in these. However, with our approximate DFT, MC simulations are needed to identify exactly what crystal phases will form.

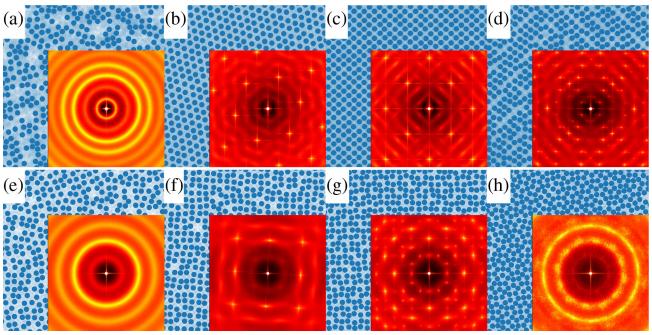


FIG. 3. Snapshots of some phases encountered in GCMC simulations [in the (x, y) plane], with fixed $[\mu(\eta), T, V]$. The respective insets show heatmap plots of the static structure factor $S(k_x, k_y)$, obtained via averaging along GCMC simulations, with color scale (different in each case) going from dark at low values to yellow at the highest values. Panels (a)–(d) are for $\lambda = 3.7$; (a) shows the liquid state at state point $\mathcal{S} = (\eta, T) = (0.35, 0.4375)$, (b) a low density hexagonal (LDHex) crystal at $\mathcal{S} = (0.425, 0.3751)$, (c) a rhombic crystal at $\mathcal{S} = (0.5, 0.25)$ and (d) a disordered smectic phase at $\mathcal{S} = (0.475, 0.4375)$. Panels (e)–(h) are for $\lambda = 2.5$; (e) shows the liquid at $\mathcal{S} = (0.4, 0.333)$, (f) a disordered low density cubic crystal at $\mathcal{S} = (0.45, 0.333)$ with wave number ratio k_3/k_2 close to $\sqrt{2}$, (g) a precursor to a 12-fold QC at $\mathcal{S} = (0.54, 0.333)$ and (h) a 12-fold QC at $\mathcal{S} = (0.6, 0.333)$.

Figure 3 shows snapshots from GCMC simulations (single box with fixed T, μ and volume V [47,48]), together with the corresponding static structure factor $S(\mathbf{k})$. The top panels are for $\lambda = 3.7$, while the bottom panels are for $\lambda = 2.5$, with average density increasing from left to right. For both λ, we observe the typical ringlike (no angular dependence) static structure factor $S(\mathbf{k}) = S(k)$ in the liquid states (a) and (e) with maxima at radii k_i. When η is increased and/or T lowered [such as in panels (a)–(c) or (e)–(f) in Fig. 3], structured phases emerge, formed from the dominant density modes already present in the liquid. They are either formed of modes with a single k_i, like the LDHex phase in Fig. 3(b), which essentially has the single length scale $2\pi/k_3$, or they originate from a coupling of two modes such as in the cubic coupling of k_2 and k_3 in (f) or rhombic k_3 and k_4 in (c), respectively. More complex structures including QCs come from having two unstable wave numbers k_i and k_j, with the requirement that corresponding wave vectors $\mathbf{k}_i$ and $\mathbf{k}_j$ add up to another already favored wave vector [26–35,52–54]. This can be seen in the QC precursor in (g) and the 12-fold QC in (h). QCs have been seen previously in HCSS systems: Refs. [22–24] present a recipe based on real-space geometric arguments for how to choose λ and η, to "design"

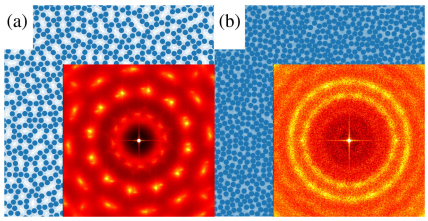


FIG. 4. (a) A 12-fold QC at $(\lambda, \epsilon, \eta) = (2.1, 5.81, 0.35)$ with wave number ratios $k_2/k_1 = 1.9225 \approx \sqrt{2+\sqrt{3}} \approx 1.932$ and $k_3/k_2 = 1.419 \approx \sqrt{2} \approx 1.414$. (b) An 18-fold QC at $(\lambda, \epsilon, \eta) = (3.42, 5.03, 0.65)$ with $k_4/k_3 = 1.289 \approx 2\sin(2\pi/9)$.

QCs, which works well at low T. Here, we extend to the present HCSS system the Fourier-space approach based on $\omega(k)$ of [27–34], which was previously developed for soft potentials. Our approach also works at higher T, near to melting, so nicely complements the low-T method of [22–24]. To tailor QCs (as foreshadowed above) one must choose η, T, and λ so that $\omega(k)$ has two unstable k_i. Both must have similar growth rates ω_i and must have k_i/k_j "close" to certain (irrational number) ratios [26–35,52–54] (explained in detail in Supplemental Material [43]). Figure 4 shows two outcomes of such a search, based on analysis of $\omega(k)$. GCMC simulations were then used to confirm the predicted 12-fold and 18-fold symmetric QCs at each of these state points, respectively.

To summarize, we have presented a versatile general approach for navigating complex phase diagrams in soft matter systems. It only requires a suitable functional $\Omega[\rho]$, from classical DFT. Via simple analysis of the dispersion relation $\omega(k)$ (obtained directly from $\Omega[\rho]$), one can easily predict where ordered (or even QC) phases are to be expected. The approach has been applied to 2D HCSS systems exhibiting up to ten emerging ordered phases; note that the theory is actually easier in 3D (where the Fourier transforms are simpler), at the cost of much more laborious simulations. Likewise, via $\omega(k)$ we can *design* potentials giving rise to specific complex crystal/QC structures, by choosing parameters to give peaks in $\omega(k)$ in certain ratios. Hand-in-hand with MC simulations, our general approach is computationally cheap and works at high T. It identifies at which state points to deploy the computationally expensive MC simulations, speeding up greatly the mapping of phase diagrams.

Acknowledgments—The authors thank Ms. Katrin Muck for her guidance related to the use of HPC. The MC computer simulation results presented here were enabled via a generous share of CPU time, offered by the Vienna Scientific Cluster (VSC) under Project No. 71263. A. J. A. gratefully acknowledges support from the EPSRC under Grant No. EP/P015689/1. This research was funded in part by the Austrian Science Fund (FWF) [Grant DOI: 10.55776/PIN8759524], gratefully acknowledged by G. K.

Data availability—The data are not publicly available. The data are available from the authors upon reasonable request.

[1] S. R. Nagel, Experimental soft-matter science, Rev. Mod. Phys. **89**, 025002 (2017).
[2] J.-L. Barrat, E. Del Gado, S. U. Egelhaaf, X. Mao, M. Dijkstra, D. J. Pine, S. K. Kumar, K. Bishop, O. Gang, A. Obermeyer *et al.*, Soft matter roadmap, J. Nonlinear Opt. Phys. Mater. **7**, 012501 (2023).
[3] J. N. Israelachvili, *Intermolecular and Surface Forces* (Academic Press, New York, 2011).
[4] W. Liu, M. Kappl, W. Steffen, and H.-J. Butt, Controlling supraparticle shape and structure by tuning colloidal interactions, J. Colloid Interface Sci. **607**, 1661 (2022).
[5] R. Ghosh Chaudhuri and S. Paria, Core/shell nanoparticles: Classes, properties, synthesis mechanisms, characterization, and applications, Chem. Rev. **112**, 2373 (2012).
[6] N. Vogel, C. Fernández-López, J. Pérez-Juste, L. M. Liz-Marzán, K. Landfester, and C. K. Weiss, Ordered arrays of gold nanostructures from interfacially assembled Au@PNIPAM hybrid nanoparticles, Langmuir **28**, 8985 (2012).
[7] M. Rey, A. D. Law, D. M. A. Buzza, and N. Vogel, Anisotropic self-assembly from isotropic colloidal building blocks, J. Am. Chem. Soc. **139**, 17464 (2017).
[8] J. Menath, J. Eatson, R. Brilmayer, A. Andrieu-Brunsen, D. M. A. Buzza, and N. Vogel, Defined core–shell particles as the key to complex interfacial self-assembly, Proc. Natl. Acad. Sci. U.S.A. **118**, e2113394118 (2021).
[9] M. Ickler, J. Menath, L. Holstein, M. Rey, D. M. A. Buzza, and N. Vogel, Interfacial self-assembly of SiO_2-PNIPAM core-shell particles with varied crosslinking density, Soft Matter **18**, 5585 (2022).
[10] Z. Li, Q. Fan, and Y. Yin, Colloidal self-assembly approaches to smart nanostructured materials, Chem. Rev. **122**, 4976 (2021).
[11] M. Dijkstra and E. Luijten, From predictive modelling to machine learning and reverse engineering of colloidal self-assembly, Nat. Mater. **20**, 762 (2021).
[12] R. Evans, The nature of the liquid-vapour interface and other topics in the statistical mechanics of non-uniform, classical fluids, Adv. Phys. **28**, 143 (1979).
[13] R. Evans, M. Oettel, R. Roth, and G. Kahl, New developments in classical density functional theory, J. Phys. Condens. Matter **28**, 240401 (2016).
[14] J. P. Hansen and I. R. McDonald, *Theory of Simple Liquids* (Academic Press, Oxford, 2013).
[15] U. M. B. Marconi and P. Tarazona, Dynamic density functional theory of fluids, J. Chem. Phys. **110**, 8032 (1999).
[16] A. J. Archer and R. Evans, Dynamical density functional theory and its application to spinodal decomposition, J. Chem. Phys. **121**, 4246 (2004).
[17] M. te Vrugt, H. Löwen, and R. Wittkowski, Classical dynamical density functional theory: From fundamentals to applications, Adv. Phys. **69**, 121 (2020).

[18] M. A. Glaser, G. M. Grason, R. D. Kamien, A. Košmrlj, C. D. Santangelo, and P. Ziherl, Soft spheres make more mesophases, Europhys. Lett. **78**, 46004 (2007).

[19] J. Dobnikar, J. Fornleitner, and G. Kahl, Ground states of model core-softened colloids, J. Phys. Condens. Matter **20**, 494220 (2008).

[20] J. Fornleitner and G. Kahl, Lane formation vs. cluster formation in two-dimensional square-shoulder systems—A genetic algorithm approach, Europhys. Lett. **82**, 18001 (2008).

[21] J. Fornleitner and G. Kahl, Pattern formation in two-dimensional square-shoulder systems, J. Phys. Condens. Matter **22**, 104118 (2010).

[22] T. Dotera, T. Oshiro, and P. Ziherl, Mosaic two-lengthscale quasicrystals, Nature (London) **506**, 208 (2014).

[23] P. Ziherl and T. Dotera, A geometric view of structure formation in soft colloids, *Proceedings of the International School of Physics "Enrico Fermi"* Vol. 193 (2016), p. 307.

[24] T. Dotera, S. Bekku, and P. Ziherl, Bronze-mean hexagonal quasicrystal, Nat. Mater. **16**, 987 (2017).

[25] H. Pattabhiraman and M. Dijkstra, On the formation of stripe, sigma, and honeycomb phases in a core–corona system, Soft Matter **13**, 4418 (2017).

[26] S. Alexander and J. McTague, Should all crystals be bcc? Landau theory of solidification and crystal nucleation, Phys. Rev. Lett. **41**, 702 (1978).

[27] K. Barkan, H. Diamant, and R. Lifshitz, Stability of quasicrystals composed of soft isotropic particles, Phys. Rev. B **83**, 172201 (2011).

[28] A. J. Archer, A. M. Rucklidge, and E. Knobloch, Quasicrystalline order and a crystal-liquid state in a soft-core fluid, Phys. Rev. Lett. **111**, 165501 (2013).

[29] K. Barkan, M. Engel, and R. Lifshitz, Controlled self-assembly of periodic and aperiodic cluster crystals, Phys. Rev. Lett. **113**, 098304 (2014).

[30] A. J. Archer, A. M. Rucklidge, and E. Knobloch, Soft-core particles freezing to form a quasicrystal and a crystal-liquid phase, Phys. Rev. E **92**, 012324 (2015).

[31] S. Savitz, M. Babadi, and R. Lifshitz, Multiple-scale structures: From Faraday waves to soft-matter quasicrystals, IUCrJ **5**, 247 (2018).

[32] D. J. Ratliff, A. J. Archer, P. Subramanian, and A. M. Rucklidge, Which wave numbers determine the thermodynamic stability of soft matter quasicrystals?, Phys. Rev. Lett. **123**, 148004 (2019).

[33] P. Subramanian, D. J. Ratliff, A. M. Rucklidge, and A. J. Archer, Density distribution in soft matter crystals and quasicrystals, Phys. Rev. Lett. **126**, 218003 (2021).

[34] A. J. Archer, T. Dotera, and A. M. Rucklidge, Rectangle-triangle soft-matter quasicrystals with hexagonal symmetry, Phys. Rev. E **106**, 044602 (2022).

[35] R. Lifshitz and D. M. Petrich, Theoretical model for Faraday waves with multiple-frequency forcing, Phys. Rev. Lett. **79**, 1261 (1997).

[36] M. Wassermair, G. Kahl, R. Roth, and A. J. Archer, Fingerprints of ordered self-assembled structures in the liquid phase of a hard-core, square-shoulder system, J. Chem. Phys. **161**, 124503 (2024).

[37] A. J. Archer, Dynamical density functional theory for dense atomic liquids, J. Phys. Condens. Matter **18**, 5617 (2006).

[38] A. J. Archer, Dynamical density functional theory for molecular and colloidal fluids: A microscopic approach to fluid mechanics, J. Chem. Phys. **130** (2009).

[39] G. Dee and J. S. Langer, Propagating pattern selection, Phys. Rev. Lett. **50**, 383 (1983).

[40] A. J. Archer, M. J. Robbins, U. Thiele, and E. Knobloch, Solidification fronts in supercooled liquids: How rapid fronts can lead to disordered glassy solids, Phys. Rev. E **86**, 031603 (2012).

[41] R. Roth, K. Mecke, and M. Oettel, Fundamental measure theory for hard disks: Fluid and solid, J. Chem. Phys. **136**, 081101 (2012).

[42] R. Roth, Fundamental measure theory for hard-sphere mixtures: A review, J. Phys. Condens. Matter **22**, 063102 (2010).

[43] See Supplemental Material at http://link.aps.org/supplemental/10.1103/nbvt-fgjy, which gives further information on $F_{\mathrm{ex}}[\rho]$ used here, the resulting analytic expression for $\hat{c}(k)$, additional discussion on instability lines, more information about our MC simulations, and details about how to identify where in parameter space to find QCs, which can be done simply using [44].

[44] Wolfram Research, Inc., Mathematica, Version 14.3 (2025), Champaign, IL.

[45] A. L. Thorneywork, S. K. Schnyder, D. G. Aarts, J. Horbach, R. Roth, and R. P. Dullens, Structure factors in a two-dimensional binary colloidal hard sphere system, Mol. Phys. **116**, 3245 (2018).

[46] GEMC consists of simulating in a pair of boxes with fixed T, μ and pressure P, allowing MC particle moves within boxes and between boxes and also the exchange of volume between boxes; further details can be found in Refs. [36,47–49]. Our MC code can be found in the GitHub digital repository: https://github.com/watermair/HCSSMC.

[47] M. P. Allen and D. J. Tildesley, *Computer Simulation of Liquids* (Oxford University Press, New York, 2017).

[48] D. Frenkel and B. Smit, *Understanding Molecular Simulation: From Algorithms to Applications* (Elsevier, New York, 2023).

[49] A. Z. Panagiotopoulos, Direct determination of phase coexistence properties of fluids by Monte Carlo simulation in a new ensemble, Mol. Phys. **61**, 813 (1987).

[50] A. Imperio and L. Reatto, Microphase separation in two-dimensional systems with competing interactions, J. Chem. Phys. **124**, 164712 (2006).

[51] W. R. Somerville, A. D. Law, M. Rey, N. Vogel, A. J. Archer, and D. M. A. Buzza, Pattern formation in two-dimensional hard-core/soft-shell systems with variable soft shell profiles, Soft Matter **16**, 3564 (2020).

[52] P. Bak, Phenomenological theory of icosahedral incommensurate ("quasiperiodic") order in Mn-Al alloys, Phys. Rev. Lett. **54**, 1517 (1985).

[53] A. M. Rucklidge, M. Silber, and A. C. Skeldon, Three-wave interactions and spatiotemporal chaos, Phys. Rev. Lett. **108**, 074504 (2012).

[54] J. K. Castelino, D. J. Ratliff, A. M. Rucklidge, P. Subramanian, and C. M. Topaz, Spatiotemporal chaos and quasipatterns in coupled reaction–diffusion systems, Physica (Amsterdam) **409D**, 132475 (2020).